Measured and Theoretical Kα X-Ray Emission Linewidths of U, Np, and Pu

Abigail Wessels,[1] Jonathan W. Dean,[1,2,*] Daniel T. Becker,[2] Douglas A. Bennett,[1] Matthew H. Carpenter,[3] Mark Croce,[3] Joseph W. Fowler,[1] Johnathon D. Gard,[2] Paul Indelicato,[4] Katrina E. Koehler,[3,5] J. A. B. Mates,[1] Daniel McNeel,[3] David Mercer,[3] Daniel R. Schmidt,[1] Katherine Schreiber,[3] Daniel S. Swetz,[1] Duc Vo,[3] Sophie Weidenbenner,[3] and Joel N. Ullom[1]

[1]*National Institute of Standards and Technology, Boulder, Colorado, USA*
[2]*University of Colorado Boulder, Boulder, Colorado, USA*
[3]*Los Alamos National Laboratory, Los Alamos, New Mexico, USA*
[4]*Laboratoire Kastler Brossel, Sorbonne Université, CNRS, ENS-PSL Research University, Collège de France, Paris, France*
[5]*Houghton University, Houghton, New York, USA*

(Received 10 December 2025; revised 16 March 2026; accepted 1 June 2026; published 10 September 2026)

We present measurements of the $K\alpha_1$ and $K\alpha_2$ natural x-ray linewidths of uranium, neptunium, and plutonium ($Z = 92, 93, 94$) obtained using a superconducting transition-edge sensor microcalorimeter array. The relative uncertainties range from 0.5% to 1.5%, improving upon previous values by factors ranging from 3 to 8. These refined linewidths reduce systematic errors in gamma-ray spectroscopy assays of Pu-bearing materials, where Kα x-rays overlap with diagnostic gamma lines. We also present multiconfiguration Dirac-Fock calculations of the Kα linewidths for U, Np, and Pu, providing a benchmark for theory and experiment. These calculations reveal a discrepancy between *ab initio* theory and experiment possible to observe only with the improved experimental accuracy achieved in this work.

DOI: 10.1103/tcbz-kqk1

Characteristic x-rays are emitted when electrons relax from an atomic energy shell to a vacancy in a lower energy shell. X-ray fundamental parameters such as emission energy, width, and line shape are element and compound specific, providing useful tools for probing atomic and molecular physics [1]. The Kα emission lines of U, Np, and Pu near 100 keV are intrinsically broad, with widths near 100 eV full width at half-maximum (FWHM), and they overlap with intense gamma-ray peaks used to identify and quantify different Pu isotopes. In this work, we make new measurements of the $K\alpha_1$ and $K\alpha_2$ linewidths of U, Np, and Pu, reducing uncertainties by up to a factor of 8. These measurements will benefit gamma-ray analysis of materials from the nuclear fuel cycle and support international nuclear safeguards by enabling more precise accounting of fissile material in nuclear facilities [2,3]. In addition to these experimental results, we make new state-of-the-art theoretical calculations to scrutinize relativistic quantum mechanics and atomic theory for the inner shells of heavy elements.

The natural Lorentzian width, γ, associated with a given x-ray transition is the sum of the level widths, Γ, of the initial and final states. These level widths are related to the decay lifetime of the state through Heisenberg's uncertainty principle, with $\Gamma_i = \hbar \sum_j A_{ji}$ for some state i; A_{ji} are the Einstein coefficients for all possible decay pathways. Each individual $\Gamma_{ji} = \hbar A_{ji}$ is known as a partial level width. These decay rates (A_{ji}) can be calculated with atomic theory and are especially complicated for large atoms with many electrons and decay pathways.

Empirically measured natural linewidths are the FWHM of the Lorentzian profile, γ, used to fit data once experimental sources of broadening have been removed. Typically, Voigt profiles are fitted to x-ray data with the Gaussian FWHM representing detector broadening and the Lorentzian FWHM being the natural linewidth [4,5]. Experimental measurements of the natural linewidths of characteristic x-rays can, therefore, be used to test the accuracy of theoretical techniques.

Previous measurements of the linewidths of U, Np, and Pu obtained with wavelength-dispersive spectrometers are several decades old [6–8] and report relative measurement uncertainties between 2% and 10%. A set of semiempirical values was tabulated in 1979 by Krause and Oliver [9] with reported uncertainties of 4%. In the present work, measurements are made using a superconducting transition-edge sensor (TES) microcalorimeter spectrometer known as SOFIA (Spectrometer Optimized for Facility Integrated Applications) [10]. Gamma-ray TESs offer high resolving power ($E/\Delta E > 1000$) and good photon collecting efficiency (> 40% photon absorption probability) at energies around 100 keV [11,12]. TESs are capable of detecting photons over a wide range of energies (in this case, up to 400 keV) without seeing a loss in resolving power. There is a growing body of work in which TESs are used to analyze nuclear materials [13,14].

*Contact author: jonathan.dean@nist.gov

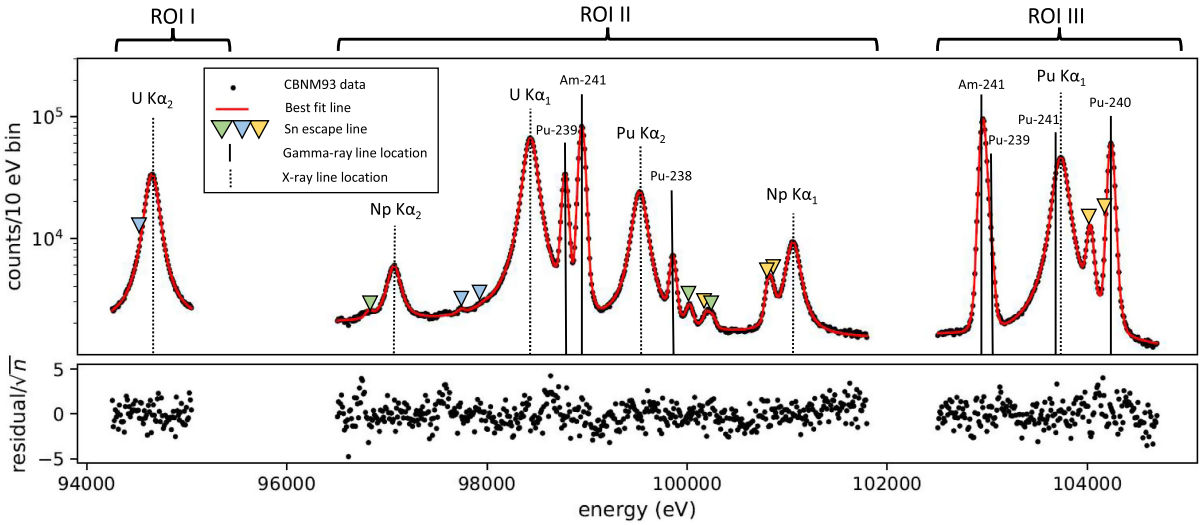

FIG. 1. Spectrum from a CBNM93 sample. Black dots are the coadded spectrum, with n being the counts per 10 eV bin. The red line is the fit from the model, which includes gamma rays (solid vertical line), x-ray lines (dotted vertical line), and Sn escape line peaks (triangles colored depending on the gamma-ray peak with yellow from 129 keV Pu-239, green from 125 keV Am-241, and blue from 123 keV Am-241). Residuals of the fit are given in the lower panel, in units of $\sigma = \sqrt{n}$. Fits and residuals for all nine datasets are shown in the Supplemental Material [24].

Previous theoretical calculations of transition rates have been published with recommended values listed in the Evaluated Atomic Data Library (EADL) [15]. Nonradiative (Auger) rates are taken from Chen *et al.* [16–18], while Scofield provides the radiative rates for the K shell [19] and the L shell [20]. Under close examination, several discrepancies within this body of work appear, indicating that the state of theoretical knowledge is less certain than the chain of references suggests. For example, the EADL gives 91.63 eV for the U K shell radiative width, whereas the cited reference in the EADL (Scofield, 1969 [19]) has the value 91.8 eV. Further complications arise when one discovers that Scofield published a paper in 1974 [21] as a correction to his 1969 [19] paper, yet this U K shell width, 93.41 eV, is even more discrepant from the EADL. For the nonradiative rates, the L shell has a greater impact on the Kα widths than the K shell, and here, we continue to see inconsistencies. The EADL cites [16], which gives nonradiative level widths for U L_1, L_2, and L_3 as 14.043 eV, 4.268 eV, and 4.571 eV, respectively, whereas the EADL reports 13.441 eV, 5.216 eV, and 4.387 eV, respectively. These are significant differences—up to 20%—that are unexplained and untraceable. The original Hartree-Slater calculations of Scofield were performed with an unpublished code whose implementation details are not available, making exact reproduction of the tabulated values difficult. Here, new theoretical values are presented to serve as a benchmark for comparisons between theory and experiment.

Data acquisition and analysis—The data for this study were acquired at Los Alamos National Laboratory. Each dataset was collected from 128 TES detectors for periods of 40 hours or less set by the requirement to thermally cycle the cryostat. Gamma-ray spectra were acquired from four different certified nuclear reference materials from the Central Bureau for Nuclear Measurements (CBNM-271) containing different mass fractions of several Pu isotopes and Am-241. Each CBNM-271 sample consists of approximately 6.6 g of PuO_2 inside a stainless steel can of diameter 40 mm and height 21 mm [22].

The U and Np x-rays are produced overwhelmingly by internal conversion after the decay of their parent nuclei, Pu and Am, respectively. The Pu x-rays are produced mainly by self-fluorescence of the mostly Pu sample; [23] contains further details on these reaction chains. Nine spectra were analyzed, including three from CBNM93 and two each from CBNM61, CBNM70, and CBNM84. One of the spectra from CBNM93 is given in Fig. 1. Information on the content of these samples, more details on the data acquisition, and an estimate of total flux and quantum efficiency are given in Supplemental Material [24].

Each TES microcalorimeter detector acts as an independent spectrometer. Data from each device are recorded as a collection of current "pulses," with each pulse's height corresponding to a photon energy. We process pulses from individual detectors and convert these data into a list of pulse heights. The list is binned into a histogram and then energy calibrated by assigning tabulated energy values to known spectral features. We then coadd the spectra from an array of individual detectors to form a single high statistics spectrum. A description of the process used to analyze raw data from a gamma-ray TES spectrometer can be found in [31]. Additional processing steps beyond those in [31] were taken. To limit distortions in our data due to pulse pileup, we cut pulses that arrived less than 60 ms after a previous pulse on the same detector. To calibrate single pixel spectra,

each of the x-ray peaks of interest was used as a calibration feature to ensure that these peaks were well aligned before coadding. Before coadding, data from detectors that achieved worse than 100 eV resolution were discarded. Spectra were fit assuming a two-Gaussian detector response function with the Gaussians having equal centroids but different widths. This response function has previously been found to be a good choice for fitting coadded spectra from detectors with different resolution values because it allows wider tails than a single Gaussian [32]. The coadded energy resolution varied among datasets taken on different days. Including this variability, the standard deviation of the primary, narrow Gaussian in the response function was 74.0 eV $\pm$ 5.5 eV FWHM at 100 keV. The uncertainty on the resolution in individual datasets was < 0.5 eV. The χ^2 of the fit was recorded for each detector, and data from detectors with a reduced χ^2 more than twice the median value were discarded. The number of detectors surviving these cuts varied from 32 to 88 between datasets. The varying number of discarded detectors depends on the quality of data taken, not on any time dependent shifts in detector quality.

The 94 keV to 105 keV region of Pu gamma-ray spectra contains many gamma-ray and x-ray peaks and is presented in Fig. 1 for a CBNM93 dataset. U and Np x-rays in Pu-bearing samples are primarily produced by internal conversion processes, while the Pu x-rays are produced by radiation induced ionization of the K shell. The data are fit with a model that consists of the sum of a background function, gamma-ray peaks, x-ray peaks, and Sn escape peaks. Gamma-ray lines arise from nuclear processes and have an intrinsic linewidth many orders of magnitude lower than the resolution of our detectors, so the observed line shape in our spectra is purely the spectrometer's detector response function. X-ray lines are modeled by convolving the natural Lorentzian line shape with the two-Gaussian detector response, resulting in the sum of two Voigt profiles. Escape peaks are due to Sn x-rays escaping the Sn absorber attached to the TES after the absorption of a high-energy photon, which results in a peak with an energy of the original peak minus the Sn x-ray energy [33].

The spectrum was fit as three smaller regions of interest (ROIs) to best model the local background level around each x-ray peak. We assumed a conventional model for the background describing the continuum, comprising primarily Compton scattering [32]. This function helps to fit regions with multiple bright gamma-ray peaks, and it creates a smoothed step function under each peak. ROI I spans (94.25 keV, 95.05 keV) and contains U Kα_2; ROI II is (96.5 keV, 101.8 keV) and contains Np K$\alpha_{1,2}$, U Kα_1, Pu Kα_2; and ROI III is (102.5 keV, 104.7 keV) and contains the Pu Kα_1 peak.

The fitting routine used here implements the Levenberg-Marquardt algorithm [34] for maximum likelihood least squares fitting, modified for Poisson-distributed data as

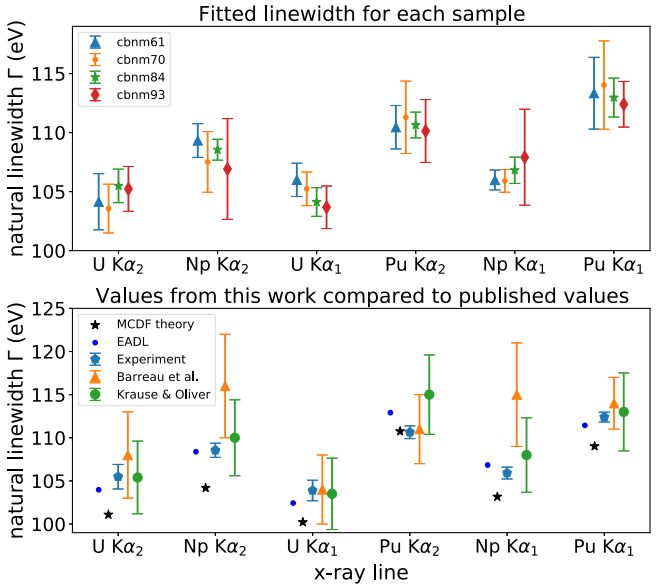

FIG. 2. Top: comparison of linewidth values from each CBNM sample. Bottom: comparing the most precise value from the present measurement (large blue circles) to published values by Krause and Oliver [9] (green circles) and Barreau *et al.* [7] (orange triangles) as well as our novel theoretical values (black stars) and those presented in the EADL (small blue circles) [15]. All error bars shown reflect 1σ confidence intervals and include statistical and systematic error estimates.

described in [35]. Data for each of the four CBNM samples were fit independently, while for each dataset, all three ROIs were fit simultaneously. The free parameters in the model are the six Lorentzian linewidths, amplitudes, and energy centroids for each x-ray line with the two Gaussian widths common to all x-ray lines. Further free parameters are the seven gamma-ray centroids and amplitudes. The amplitudes of the Sn escape peaks are free, but the centroids are fixed to the centroids of the gamma-ray or x-ray lines minus the literature values for Sn Kα_1, Kα_2, Kβ_1, and Kβ_3 from [36]. The linear background has two free parameters for each of the three ROIs.

The linewidth results from all datasets for each of the four CBNM samples were combined as a weighted mean using the inverse square of the statistical error from each value as the weights. These results are plotted in Fig. 2. We assessed the statistical and systematic errors of each line for each sample and chose the lowest total uncertainty value as our recommended value for each x-ray line. We chose not to combine results from different samples, because they each had a different systematic error, and we found evidence that the systematic errors for certain lines were correlated between samples; more information on this is included in Supplemental Material. To combine these results with a weighted mean based on total uncertainty would be incorrect because of this correlation, and it would produce biased results. For the case of U Kα_1, final values for two samples had approximately the same total

TABLE I. Linewidth values for U, Np, and Pu Kα_1 and Kα_2 from this work, theory and experiment, and from previous published values. Krause and Oliver [9] values are semiempirical. The EADL values [15] are theoretical. Barreau *et al.* [7]; Nelson, John, and Saunders [6]; and Kessler *et al.* [8] are experimental values measured with wavelength-dispersive spectrometers. All units are eV, and uncertainties are shown in cases where they were reported.

U Kα_2	Np Kα_2	Pu Kα_2	U Kα_1	Np Kα_1	Pu Kα_1	Ref.
105.49 ± 1.42	108.55 ± 0.82	110.64 ± 0.74	103.89 ± 1.19	105.91 ± 0.69	112.40 ± 0.57	This Letter, experimental
101.09	104.19	110.75	100.22	103.47	109.02	This Letter, theory
103.97	108.38	112.9	102.44	106.85	111.38	EADL values [15]
105.4 ± 4.2	110 ± 4.4	115 ± 4.6	103.5 ± 4.1	108 ± 4.3	113 ± 4.5	Krause and Oliver [9]
109.0 ± 10.90	106.5 ± 10.65	116.4 ± 11.64	106.8 ± 10.68	97.8 ± 9.78	115.7 ± 11.57	Nelson, John, and Saunders [6]
108 ± 5	116 ± 6	111 ± 4	104 ± 4	115 ± 6	114 ± 3	Barreau *et al.* [7]
106.3 ± 6.1			103.9 ± 2.4			Kessler *et al.* [8]

uncertainty, so we averaged these values and report that final value. We present recommended values with uncertainties for each x-ray line in Table I and Fig. 2.

Uncertainty analysis—The statistical uncertainties derived from this analysis are the standard errors from the fitting procedure without rescaling the covariance matrix based on the goodness of fit. After combining all datasets for each sample, the linewidth values have statistical uncertainties < 1 eV for all lines.

The systematic uncertainties of this analysis are less straightforward to quantify. They are also challenging to combine, as they are correlated between different spectra, which are fit with the same method. We considered and evaluated the five sources of systematic uncertainty listed here: (1) broadening due to peak misalignment when coadding single detector spectra; (2) presence of multiple isotopes with different peak energies; (3) dependence on ROI limits used for the fits; (4) imperfect detector response function model; (5) sample to sample variation. Estimated values for each uncertainty and detailed information about how each source of uncertainty was evaluated can be found in Supplemental Material.

The third item was the dominant uncertainty for most lines. We found that by varying the energy range of data that we fit over, we could vary the goodness-of-fit and parameter values. We investigated the magnitude of this effect by repeating our fits with five different data ranges and measuring the range in which each linewidth varied as a result. This effect comes from using a simplified background model and an imperfect detector response model and is an avenue for future work.

New calculations of the Kα *x-ray linewidths*—Along with the empirical measurements, we provide theoretical calculations of the Kα_1 and Kα_2 natural linewidths, γ, of U, Np, and Pu. As mentioned, this involves obtaining the partial level widths, and therefore rates, for all possible decays of the initial and final states. The calculations are performed with the multiconfiguration Dirac-Fock (MCDF) method [37–39] implemented in the MCDF and general matrix elements (MCDFGME) program code [40–42]. Atomic U and Np have both $4f$ and $6d$ open shells, and Pu has a $4f$ open shell, leading to a large number of possible levels and complex calculations. However, this structure is not applicable here, since the measurements were done for elements contained in a solid, which modifies their outer shell structure. We have, therefore, performed calculations with entirely closed shells. This should have a negligible effect, as has been checked in previous energy evaluations [36,43]. In evaluating radiative transition rates, both the initial and final state wave functions are fully relaxed, and nonorthogonality between the relaxed wave functions is handled exactly [44]. The energy contains all known QED corrections to order α/π and $(\alpha/\pi)^2$, where α is the fine-structure constant, and self-energy screening is included using the effective operator described in [45,46].

The Kα_1 (Kα_2) natural linewidth is the sum of the lifetime level width of the K (K) shell and the L_3 (L_2) subshell. Two decay mechanisms are considered, radiative and nonradiative (Auger) decay. Electron decays from levels up to the O ($n = 5$) shell are considered, including electric and magnetic dipole, quadrupole, and octupole transitions. Forbidden transitions have negligible partial widths, and the impact of transitions decreases with increasing Δn. For nonradiative transitions, we consider Auger transitions KXY, L_2XY, and L_3XY for X, $Y \in \{L, M, N\}$, where X represents the shell that the relaxing electron originates from, and Y represents the shell that the ejected electron originates from. Similar to the radiative transitions, relaxations involving the next shell up from the initial hole are dominant, with negligible contributions from KNN and LNN Auger transitions. Table II shows the calculated lifetime level widths and compares them to published values. These level widths are then used to calculate the linewidths reported in Table I.

Results—Table I and Fig. 2 compare the theoretical, empirical, and semiempirical results from this work to previous published values. All results agreed to within 2σ confidence intervals with the semiempirical values of Krause and Oliver [9] and the empirical from Barreau *et al.* [7]. Our work's reported uncertainties are significantly lower than those for other published measured values.

These calculations have been undertaken in a fully relativistic framework with QED corrections to second

TABLE II. Theoretical results for radiative (Rad.), nonradiative (Auger), and total level widths with comparisons to EADL recommended values [15], experiment [47], and semiempirical values [9]. All values are reported in eV.

	This Letter			Ref. [15]	Ref. [47]	Ref. [9]
	Rad.	Auger	Total	Total	Total	Total
U K	92.16	2.14	94.30	94.46		96.10
U L_2	4.37	2.42	6.79	9.51	8.5	9.32
U L_3	3.67	2.25	5.92	7.97	8.4	7.43
Np K	96.21	1.52	97.73	98.63		100.00
Np L_2	4.62	1.84	6.46	9.75		9.91
Np L_3	3.76	1.98	5.74	8.21		7.59
Pu K	100.40	2.26	102.67	102.92		105.00
Pu L_2	4.87	3.21	8.08	9.99		10.50
Pu L_3	4.06	2.30	6.35	8.47		7.82

order. These calculations seem to have underpredicted the linewidths across all measurements, except for Pu Kα_2. This is to be expected. Deriving linewidths solely from the decay rates of the initial and final states necessarily misses some effects that increase the linewidth. We hypothesize four independent effects that lead to broadening not captured by isolated atomic theory from decay rates. First, shakeoff satellite lines occur when a secondary electron is ejected during the initial K shell ionization, altering the potential that the Kα transition takes place in and leading to a nondegenerate transition energy. The satellite transitions can be close to the main, or diagram, line and not well resolved, leading to asymmetries and broader than expected lines [48,49]. Another possibility is that the satellite lines are well resolved, such as the K$\alpha_{3,4}$ line [50,51]. For U, shakeoff satellites have been shown to increase the natural linewidth of uranium M-lines [52]. Anagnostopoulos *et al.* [53] measured shakeoff satellite lines for U Kα using 500 MeV Ne^{8+} as the excitation source and observed a U Kα_1 width of 118 eV. With such a high-energy, ionic excitation source, satellite line intensities are inflated, leading to a significant increase in observed width. The nuclear decays in the CBNM reference materials used in this work range from just above the K-edge of the target elements to roughly 1 MeV. At these energies, the shakeoff satellites would be far less intense than those observed in Anagnostopoulos *et al.* [53], yet would still add some width to the Kα transitions. Second, depending on the specific isotope and its magnetic moment, there may be hyperfine splitting of order 1 eV. Third, our approximation of an entirely closed electron configuration removes nondegenerate transitions of the diagram (i.e., no shakeoff) line that arise due to the multiple quantum states that unpaired electrons exist in. For medium Z elements where unpaired electrons exist in the M or N shell, this effect can be of the order 1 eV [48,49]. We expect this latter effect to be minimal for the transitions considered in this work due to the unpaired electrons existing in the O shell. Fourth, a recent work [54] has demonstrated that x-ray emission rates relative to nonradiative rates can depend on the environment, which is not accounted for in our isolated atomic theory. Each of these three effects is an avenue for future computational work.

Conclusions—This work has provided new empirical and theoretical values for the Kα x-ray linewidths of U, Np, and Pu. The six linewidths in this work have uncertainties between 0.5% and 1.5%, marking an improvement over previous studies ranging from a factor of 3 to a factor of 8. This improvement was enabled by the use of a TES spectrometer with wide dynamic range and high resolving power. The previous theoretical tabulations are neither traceable nor reproducible. There are good reasons that *ab initio* widths resulting from decay rate calculations should underpredict the empirical widths, as they do not account for shakeoff satellite lines. Our theory results match this expectation, predicting a natural lifetime width roughly 1% to 4% smaller than observed. Future work should include theoretically derived shakeoff satellite lines and consider isotopic shifts and structure in the diagram lines. These calculated transitions should be used to fit to the data to account for all effects that increase broadening beyond the lifetime width.

We have shown that TESs are capable of making metrological measurements in the 100 keV energy range, and we anticipate extending these efforts in the future to improve on a range of other fundamental parameters needed for accurate nuclear materials analysis using gamma-ray spectroscopy.

Acknowledgments—The authors gratefully acknowledge the support of the U.S. Department of Energy through the NE and NEUP programs; this work is published as LA-UR-25-30180. A. W. is supported by the National Research Council Post-Doctoral Fellowship. This work was performed under financial assistance Award No. 70NANB23H027 from the U.S. Department of Commerce, National Institute of Standards and Technology.

Data availability—The data that support the findings of this article are not publicly available because of legal restrictions preventing unrestricted public distribution. The data are available from the authors upon reasonable request.

[1] M. Guerra, M.-C. Lépy, J. P. Santos, and B. Beckhoff, Radiat. Phys. Chem. **212**, 111097 (2023).

[2] L. A. N. Laboratory, Technical References—Los Alamos National Laboratory—lanl.gov, https://www.lanl.gov/engage/training/safeguards-and-security-training/technical-references, [Accessed 03-03-2026].

[3] A. Hoover, R. Winkler, M. Rabin, D. Bennett, W. Doriese, J. Fowler, J. Hayes-Wehle, R. Horansky, C. Reintsema, D. Schmidt *et al.*, IEEE Trans. Nucl. Sci. **61**, 2365 (2014).

[4] J. W. Dean, H. A. Melia, C. T. Chantler, and L. F. Smale, J. Phys. B **52**, 165002 (2019).

[5] J. W. Fowler, G. C. O'Neil, B. K. Alpert, D. A. Bennett, E. V. Denison, W. Doriese, G. C. Hilton, L. T. Hudson, Y.-I. Joe, K. M. Morgan *et al.*, Metrologia **58**, 015016 (2021).

[6] G. Nelson, W. John, and B. Saunders, Phys. Rev. **187**, 1 (1969).

[7] G. Barreau, H. Börner, T. von Egidy, and R. W. Hoff, Z. Phys. A **308**, 209 (1982).

[8] E. G. Kessler Jr., R. D. Deslattes, D. Girard, W. Schwitz, L. Jacobs, and O. Renner, Phys. Rev. A **26**, 2696 (1982).

[9] M. O. Krause and J. Oliver, J. Phys. Chem. Ref. Data **8**, 329 (1979).

[10] M. Croce, D. Henzlova, H. Menlove, D. Becker, and J. Ullom, J. Nucl. Mater. Manage. **49**, 116 (2021), https://www.ingentaconnect.com/content/inmm/jnmm/2021/00000049/00000001/art00009.

[11] D. Bennett, R. Horansky, D. Schmidt, A. Hoover, R. Winkler, B. Alpert, J. Beall, W. Doriese, J. Fowler, C. Fitzgerald *et al.*, Rev. Sci. Instrum. **83**, 093113 (2012).

[12] J. Ullom and D. Bennett, Supercond. Sci. Technol. **28**, 084003 (2015).

[13] K. Nakamura, K. Maehata, T. Sugimoto, Y. Kiguchi, N. Iyomoto, Y. Morishita, K. Takasaki, and K. Mitsuda, Prog. Nucl. Sci. Technol. **6**, 8 (2019).

[14] K. A. Schreiber, K. E. Koehler, M. P. Croce, E. N. Stark, D. G. McNeel, M. H. Carpenter, D. J. Mercer, E. P. Abel, B. Archambault, L. Arrigo *et al.*, Front. Nucl. Eng. **4** (2025).

[15] S. Perkins, D. Cullen, M. Chen, J. Rathkopf, J. Scofield, and J. Hubbell, Tech. Rep., Lawrence Livermore National Lab., CA (United States), 1991, https://www.iaea.org/resources/databases/photon-and-electron-interaction-data.

[16] M. H. Chen, E. Laiman, B. Crasemann, M. Aoyagi, and H. Mark, Phys. Rev. A **19**, 2253 (1979).

[17] M. H. Chen, B. Crasemann, and H. Mark, Phys. Rev. A **21**, 436 (1980).

[18] M. H. Chen, B. Crasemann, and H. Mark, Phys. Rev. A **24**, 177 (1981).

[19] J. H. Scofield, Phys. Rev. **179**, 9 (1969).

[20] J. Scofield, Phys. Rev. A **10**, 1507 (1974).

[21] J. Scofield, Phys. Rev. A **9**, 1041 (1974).

[22] Central Bureau for Nuclear Measurements (CBNM), Certificate of analysis: CBNM nuclear reference material 271 (PuO2), Joint Research Centre, Commission of the European Communities, Geel, Belgium (1987), certified isotopic composition of plutonium oxide reference material, URL https://nds.iaea.org/media-idb/certificates/Pu_CBNM271.pdf.

[23] H. Willmes, T. Ando, and R. J. Gehrke, Int. J. Appl. Radiat. Isot. **36**, 123 (1985).

[24] See Supplemental Material at http://link.aps.org/supplemental/10.1103/tcbz-kqk1 for additional information on data acquisition and analysis, the CBNM sample information and quality of fits, and evaluating uncertainties in fitted linewidths. This includes References [25–30].

[25] National Nuclear Data Center, Brookhaven National Laboratory, NuDat (Nuclear Structure and Decay Data), WWW Document (2008), accessed: March 2, 2026, URL https://www.nndc.bnl.gov/nudat3/.

[26] T. Kibédi, T. Burrows, M. Trzhaskovskaya, P. Davidson, and C. Nestor, Nucl. Instrum. Methods Phys. Res., Sect. A **589**, 202 (2008).

[27] J. Hubbell and S. Seltzer, Tables of x-ray mass attenuation coefficients and mass energy-absorption coefficients 1 keV to 20 meV for elements $Z = 1$ to 92 and 48 additional substances of dosimetric interest (1995), accessed: March 2, 2026.

[28] J. A. Bearden, Rev. Mod. Phys. **39**, 78 (1967).

[29] National Nuclear Data Center, National Nuclear Data Center, https://www.nndc.bnl.gov/ (2023), [Online; accessed 13-September-2023], URL https://www.nndc.bnl.gov/.

[30] G. Zschornack, *Handbook of X-ray Data* (Springer Science & Business Media, New York, 2007).

[31] D. T. Becker, B. K. Alpert, D. A. Bennett, M. P. Croce, J. W. Fowler, J. D. Gard, A. S. Hoover, Y. I. Joe, K. E. Koehler, J. A. Mates *et al.*, IEEE Trans. Nucl. Sci. **66**, 2355 (2019).

[32] A. Hoover, R. Winkler, M. Rabin, D. Vo, J. Ullom, D. Bennett, W. Doriese, J. Fowler, R. Horansky, D. Schmidt *et al.*, IEEE Trans. Nucl. Sci. **60**, 681 (2013).

[33] M. D. Yoho, K. E. Koehler, D. T. Becker, D. A. Bennett, M. H. Carpenter, M. P. Croce, J. D. Gard, J. Mates, D. J. Mercer, N. J. Ortiz *et al.*, Nucl. Instrum. Methods Phys. Res., Sect. A **977**, 164307 (2020).

[34] M. Newville, T. Stensitzki, D. Allen, M. Rawlik, A. Ingargiola, and A. Nelson, Astrophysics Source Code Library, ascl–1606 (2016).

[35] J. W. Fowler, J. Low Temp. Phys. **176**, 414 (2014).

[36] R. Deslattes, E. K. Jr., P. Indelicato, L. de Billy, E. Lindroth, and J. Anton, Rev. Mod. Phys. **75**, 35 (2003).

[37] I. P. Grant, Adv. Phys. **19**, 747 (1970).

[38] J. P. Desclaux, Comput. Phys. Commun. **9**, 31 (1975).

[39] J. P. Desclaux, J. Dolbeault, M. J. Esteban, P. Indelicato, and E. Séré, in *Computational Chemistry*, edited by C. Le Bris and M. De Franceschi (Elsevier, New York, 2003), vol. X of Handbook of Numerical Analysis, p. 1032.

[40] J. P. Desclaux, in *Methods and Techniques in Computational Chemistry*, edited by E. Clementi (STEF, Cagliary, 1993), vol. A: Small Systems of *METTEC*, p. 253.

[41] P. Indelicato and J. Desclaux, MCDFGME, a MultiConfiguration Dirac Fock and General Matrix Elements program (release 2005), http://kroll.lkb.upmc.fr/mcdf (2005).

[42] P. Indelicato, MCDFGME: A multiconfiguration Dirac-Fock and general matrix elements program (release 2022) (2022), http://www.lkb.upmc.fr/metrologysimplesystems/mdfgme-a-general-purpose-multiconfiguration-dirac-foc-program.

[43] P. Indelicato, S. Boucard, and E. Lindroth, Eur. J. Phys. D **3**, 29 (1998).

[44] P. Indelicato, Hyperfine Interact. **108**, 39 (1997).

[45] V. M. Shabaev, I. I. Tupitsyn, and V. A. Yerokhin, Phys. Rev. A **88**, 012513 (2013).

[46] A. V. Malyshev, D. A. Glazov, V. M. Shabaev, I. I. Tupitsyn, V. A. Yerokhin, and V. A. Zaytsev, Phys. Rev. A **106**, 012806 (2022).

[47] P.-A. Raboud, J.-Cl. Dousse, J. Hoszowska, and I. Savoy, Phys. Rev. A **61**, 012507 (1999).

[48] J. W. Dean, H. A. Melia, T. V. B. Nguyen, and C. T. Chantler, Phys. Rev. A **109**, 022809 (2024).

[49] J. W. Dean, S. N. Thompson, and C. T. Chantler, Molecules **29** (2024).
[50] H. A. Melia, J. W. Dean, T. V. B. Nguyen, and C. T. Chantler, Phys. Rev. A **107**, 012809 (2023).
[51] D. Sier, J. W. Dean, N. T. T. Tran, T. Kirk, C. Q. Tran, J. F. W. Mosselmans, S. Diaz-Moreno, and C. T. Chantler, IUCrJ **11**, 620 (2024).
[52] J. Starosta, M. Polasik, and K. Słabkowska, Phys. Scr. **2013**, 014021 (2013).
[53] D. F. Anagnostopoulos, G. L. Borchert, D. Gotta, and K. Rashid, Z. Phys. D **18**, 139 (1991).
[54] J. Hofierka and L. S. Cederbaum, Radiat. Phys. Chem. **239**, 113343 (2026).